Simulated all-sky maps of the weak gravitational lensing distortion of the CMB

Carmelita Carbone[1,2]⋆, Volker Springel[3], Carlo Baccigalupi[1], Matthias Bartelmann[4], Sabino Matarrese[5]

[1] *SISSA/ISAS, Astrophysics Sector, Via Beirut 4, I-34014, Trieste, Italy and*
INFN, Sezione di Trieste, Via Valerio, 2, 34127, Trieste, Italy
[2] *Institut de Ciències de l'Espai, CSIC/IEEC, Campus UAB, F. de Ciències, Torre C5 par-2, Barcelona 08193, Spain*
[3] *Max-Planck-Institute for Astrophysics, Karl-Schwarzschild-Str. 1, D-85741 Garching, Germany*
[4] *Institut für Theoretische Astrophysik, Universität Heidelberg, Tiergartenstrasse 15, D-69121, Heidelberg, Germany*
[5] *Dipartimento di Fisica 'Galileo Galilei', Università di Padova and*
INFN, Sezione di Padova, Via Marzolo 8, I-35131 Padova, Italy

16 November 2007

ABSTRACT
We use the large cosmological Millennium Simulation (MS) to construct the first all-sky maps of the lensing potential and the deflection angle, aiming at gravitational lensing of the CMB. Exploiting the Born approximation, we implement a map-making procedure based on direct ray-tracing through the gravitational potential of the MS. We stack the simulation box in redshift shells up to $z \sim 11$, producing continuous all-sky maps with arcminute angular resolution. A randomization scheme avoids repetition of structures along the line of sight. The angular power spectra of the projected lensing potential and the deflection-angle modulus agree well with semi-analytic estimates on scales between a few arcminutes and about one degree. We find a deficit in power on large scales and an excess in the deflection-angle power on small scales, which we interpret as due to non-linear clustering in the MS. Our map-making procedure is ideally suited for studying lensing of CMB anisotropies, for analyzing cross-correlations with foreground structures, or other secondary CMB anisotropies such as the Rees-Sciama effect.

Key words: gravitational lensing, cosmic microwave background, cosmology

1 INTRODUCTION

The cosmic microwave background (CMB) is characterized both by primary anisotropies, imprinted at the last scattering surface, and by secondary anisotropies caused along the way to us by density inhomogeneities and re-scatterings on electrons that are freed during the epoch of reionization, and heated to high temperature when massive structures virialize. One of the interesting effects that can generate secondary anisotropies is the weak gravitational lensing of the CMB, which arises from the distortions induced in the geodesics of CMB photons by gradients in the gravitational matter potential (Bartelmann & Schneider 2001; Lewis & Challinor 2006). Forthcoming CMB probes do have the sensitivity and expected instrumental performance which may allow a detection of the lensing distor-

tions of the primary CMB anisotropies, which would then also provide new insights and constraints on the expansion history of the universe and on the process of cosmological structure formation (Acquaviva & Baccigalupi 2006; Hu *et al.* 2006). However, accurate predictions for the expected anisotropies in total intensity and polarization are clearly needed for analyzing this future data, which demands for detailed simulated maps.

The increasing availability of high-resolution N-body simulations in large periodic volumes makes it possible to directly simulate the CMB distortions caused by weak lensing using realistic cosmological structure formation calculations. This work represents a first step in that direction. Existing studies already give access to statistical properties of the expected CMB lensing signal, such as the two-point correlation function and power spectrum of the lensing potential and deflection angle, see e.g. Lewis (2005) and references therein. This is based on 'semi-analytic' calculations that

⋆ E-mail: carbone@ieec.uab.es

use approximate parameterizations of the non-linear evolution of the matter power spectrum. However, our approach of propagating rays through the forming dark matter structures gives access to the full statistics of the signal, including non-linear and non-Gaussian effects. Furthermore, it allows the accurate characterization of correlations of CMB lensing distortions with the cosmic large-scale structure, and with other foregrounds such as the Sunyaev-Zeldovich and Rees-Sciama effects. Hopefully this will allow improvements in the methods for separating the different contributions to CMB anisotropies in the data, which would be of tremendous help to uncover all the cosmological information in the forthcoming observations.

From an experimental point of view, the improved precision of the CMB observations, in particular that of the next generation experiments[1], may in fact require an accurate delensing methodology and a detailed lensing reconstruction. CMB experiments targeting for instance the CMB polarization, and in particular the curl component of the polarization tensor, the so called *B*-modes from cosmological gravitational waves, may greatly benefit from a precise knowledge of the lensing effects in order to separate them from the primordial cosmological signal (Seljak & Hirata 2004). In particular, for a correct interpretation of the data from the forthcoming Planck satellite[2], it will be absolutely essential to understand and model the CMB lensing, as the satellite has the sensitivity and overall instrumental performance for measuring the CMB lensing with good accuracy. We note that a first detection of CMB lensing in data from the Wilkinson Microwave Anisotropy Probe (WMAP[3]) together with complementary data has already been claimed by Smith *et al.* (2007).

In this study we introduce a new methodology for the construction of all-sky lensing-potential and deflection-angle maps, based on a very large cosmological simulation, the *Millennium* run (Springel *et al.* 2005). As a first step in the analysis of the produced maps we focus on determining the interval of angular scales for which the simulated maps matches the semi-analytical expectations. This will in particular inform about the largest scales that are still trustworthy in our maps, which is important since we expect a lack of lensing power on large scales, due to the finite volume of the N-body simulation. At the other extreme, at the smallest resolved scales, we are interested in the question whether our maps show evidence for extra lensing power due to the accurate representation of higher-order non-linear effects in our simulation methodology. On these small scales, the impact of non-Gaussianities from the mapping of non-linear lenses is expected to be largest.

This paper is organized as follows. In Section 2, we briefly describe the basic aspects of lensing relevant to our work. In Section 3, we describe the N-body simulation and the details of our map-making procedure. In Section 4, we present the lensing-potential and deflection-angle maps, and study the distribution of power in the angular domain. In Section 5 we provide a summary and discussion.

2 LENSED MAPS OF THE CMB VIA THE BORN APPROXIMATION

In what follows we will consider the *small-angle scattering* limit, *i.e.* the case where the *change* in the comoving separation of CMB light-rays, owing to the deflection caused by gravitational lensing from matter inhomogeneities, is small compared to the comoving separation of the *undeflected* rays. In this case it is sufficient to calculate all the relevant integrated quantities, *i.e.* the so-called *lensing-potential* and its angular gradient, the *deflection-angle*, along the undeflected rays. This small-angle scattering limit corresponds to the so-called "Born approximation".

We treat the CMB last scattering as an instantaneous process and neglect reionization. Adopting conformal time and comoving coordinates in a flat geometry (Ma *et al.* 1995), the integral for the projected lensing-potential due to scalar perturbations with no anisotropic stress reads

$$\Psi(\hat{\mathbf{n}}) \equiv -2 \int_0^{r_*} \frac{r_* - r}{r_* r} \frac{\Phi(r\hat{\mathbf{n}}; \eta_0 - r)}{c^2} \, \mathrm{d}r \,, \qquad (1)$$

while the corresponding deflection-angle integral is

$$\boldsymbol{\alpha}(\hat{\mathbf{n}}) \equiv -2 \int_0^{r_*} \frac{r_* - r}{r_* r} \nabla_{\hat{\mathbf{n}}} \frac{\Phi(r\hat{\mathbf{n}}; \eta_0 - r)}{c^2} \, \mathrm{d}r \,, \qquad (2)$$

where r is the comoving distance, $r_* \simeq 10^4$ Mpc is its value at the last-scattering surface, η_0 is the present conformal time, Φ is the physical peculiar gravitational potential generated by density perturbations, and $[1/r]\nabla_{\hat{\mathbf{n}}}$ is the two dimensional (2D) transverse derivative with respect to the line-of-sight pointing in the direction $\hat{\mathbf{n}} \equiv (\vartheta, \varphi)$ (Hu 2000; Bartelmann & Schneider 2001; Refregier 2003; Lewis & Challinor 2006).

Actually, the lensing potential is formally divergent owing to the $1/r$ term near $r = 0$; nonetheless, this divergence affects the lensing potential monopole only, which can be set to zero, since it does not contribute to the deflection-angle. In this way the remaining multipoles take a finite value and the lensing potential field is well defined (Lewis & Challinor 2006). Analytically, the full information about the deflection angle is contained in the lensing potential, but numerically the two equations (1) and (2) are generally not equivalent, and it will typically be more accurate to solve the integral (2) directly to obtain the deflection angle instead of finite-differencing the lensing potential.

If the gravitational potential Φ is Gaussian, the lensing potential is Gaussian as well. However, the lensed CMB is non-Gaussian, as it is a second order cosmological effect produced by cosmological perturbations onto CMB anisotropies, yielding a finite correlation between different scales and thus non-Gaussianity. This is expected to be most important on small scales, due to the non-linearity already present in the underlying properties of lenses.

The most advanced approach developed so far for the construction of all-sky lensed CMB maps (Lewis 2005) employs a semi-analytical modeling of the non-linear power spectrum (Smith *et al.* 2003), and derives from that the lensing potential and deflection angle templates assuming Gaussianity. This approach is therefore accurate for what concerns the two point correlation function of the lensing potential, as long as the non-linear two-point power of the matter is modeled correctly, but it ignores the influence of any statistics of higher order, which is expected to become
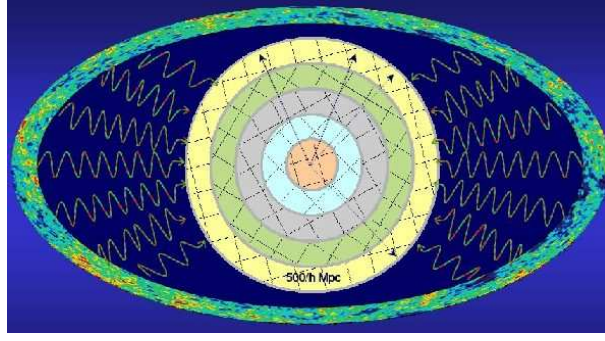
Figure 1. Sketch of the adopted stacking and randomization process. The passage of CMB photons through the dark matter distribution of the Universe is followed by stacking the gravitational potential boxes of the MS, which are $500\,h^{-1}\mathrm{Mpc}$ on a side (comoving). Shells of thickness $500\,h^{-1}\mathrm{Mpc}$ are filled with periodic replicas of the box. All boxes (squares) that fall into the same shell are randomized with the same coordinate transformation (rotation and translation), which, in turn, differs from shell to shell.

relevant on small scales, where the non-linear power is most important. The use of N-body simulations to calculate the lensing has the advantage to possess a built-in capability of accurately taking into account *all* the effects of non-linear structure formation. On the other hand, the use of N-body simulations also faces limitations due to their limited mass and spatial resolution, and from their finite volume, as we will discuss later on in more detail.

For what concerns the line-of-sight integration in Eqs. (1) and (2), the Born-approximation along the *unde-flected* photon path holds to good accuracy and allows to obtain results which include the non-linear physics. Even on small scales, in fact, this approximation can be exploited in the small-angle scattering limit, *i.e.* for typical deflections being of the order of arcminutes or less (Hirata & Seljak 2003; Shapiro & Cooray 2006). For example, a single cluster typically gives deflection angles of a few arcminutes, while smaller structures, such as galaxies, lead to arcsecond deflections. Furthermore, it can be shown that the Born-approximation also holds in 'strong' lensing cases, provided that the deflection angles are equally small. Finally, second order corrections to the Born approximation (for instance a non-vanishing curl component) are expected to be subdominant with respect to the non-linear structure evolution effects on small scales (Lewis & Challinor 2006). For these reasons, we argue that this approximation should be accurate enough for calculating all-sky weak lensing maps of the CMB based on cosmological N-body simulations.

3 MAP-MAKING PROCEDURE FOR THE MILLENNIUM SIMULATION

The Millennium Simulation (MS) is a high-resolution N-body simulation carried out by the Virgo Consortium (Springel *et al.* 2005). It uses $N = 2160^3 \simeq 1.0078 \times 10^{10}$ collisionless particles, with a mass of $8.6 \times 10^8\,h^{-1}\mathrm{M_\odot}$, to follow structure formation from redshift $z = 127$ to the present, in a cubic region $500\,h^{-1}\mathrm{Mpc}$ on a side, and with periodic boundary conditions. Here h is the Hubble constant in units of $100\,\mathrm{km\,s^{-1}Mpc^{-1}}$. With ten times as many particles as the previous largest computations of this kind (Colberg *et al.* 2000; Evrard *et al.* 2002; Wambsganss *et al.*

2004), it features a substantially improved spatial and time resolution within a large cosmological volume.

The cosmological parameters of the MS are as follows. The ratio between the total matter density and the critical one is $\Omega_m = 0.25$, of which $\Omega_b = 0.045$ is in baryons, while the density of cold dark matter (CDM) is given by $\Omega_{\mathrm{CDM}} = \Omega_m - \Omega_b$. The spatial curvature is assumed to be zero, with the remaining cosmological energy density made up by a cosmological constant, $\Omega_\Lambda = 0.75$. The Hubble constant is taken to be $H_0 = 73\,\mathrm{km\,s^{-1}Mpc^{-1}}$. The primordial power spectrum of density fluctuations in Fourier space is assumed to be a simple scale-invariant power law of wavenumber, with spectral index $n_s = 1$. Its normalization is set by the rms fluctuations in spheres of radius $8h^{-1}$ Mpc, $\sigma_8 = 0.9$, in the linearly extrapolated density field at the present epoch. The adopted parameter values are consistent with a combined analysis of the 2dF Galaxy Redshift Survey (2dFGRS) and the first year WMAP data (Colless *et al.* 2001; Spergel *et al.* 2003).

Thanks to its large dynamic range, the MS has been able to determine the non-linear matter power spectrum over a larger range of scales than possible in earlier works (Jenkins *et al.* 1998). Almost five orders of magnitude in wavenumber are covered (Springel *et al.* 2005). This is a very important feature for studies of CMB lensing, as we expect that this dynamic range can be leveraged to obtain access to the full non-Gaussian statistics of the lensing signal, limited only by the volume of the Millennium simulation and the maximum angular resolution resulting from its gravitational softening length and particle number. We stress again that the lensed CMB is non-Gaussian even if the underlying lenses do possess a Gaussian distribution. Moreover, the non-linear evolution of large scale structures produces a degree of non-Gaussianity in the lenses distribution which contributes to the non-Gaussian statistics of the lensed CMB on small scales. This non-Gaussian contribution can be computed only via the use of N-body simulations which are able to accurately describe the non-linear evolution of the lenses. These non-linearities are known to alter the lensed temperature power spectrum of CMB anisotropies by about $\sim 0.2\%$ at $\ell \sim 2000$ and by $\sim 1\%$ or more on smaller scales. But, much more notably, they introduce $\sim 10\%$ corrections to
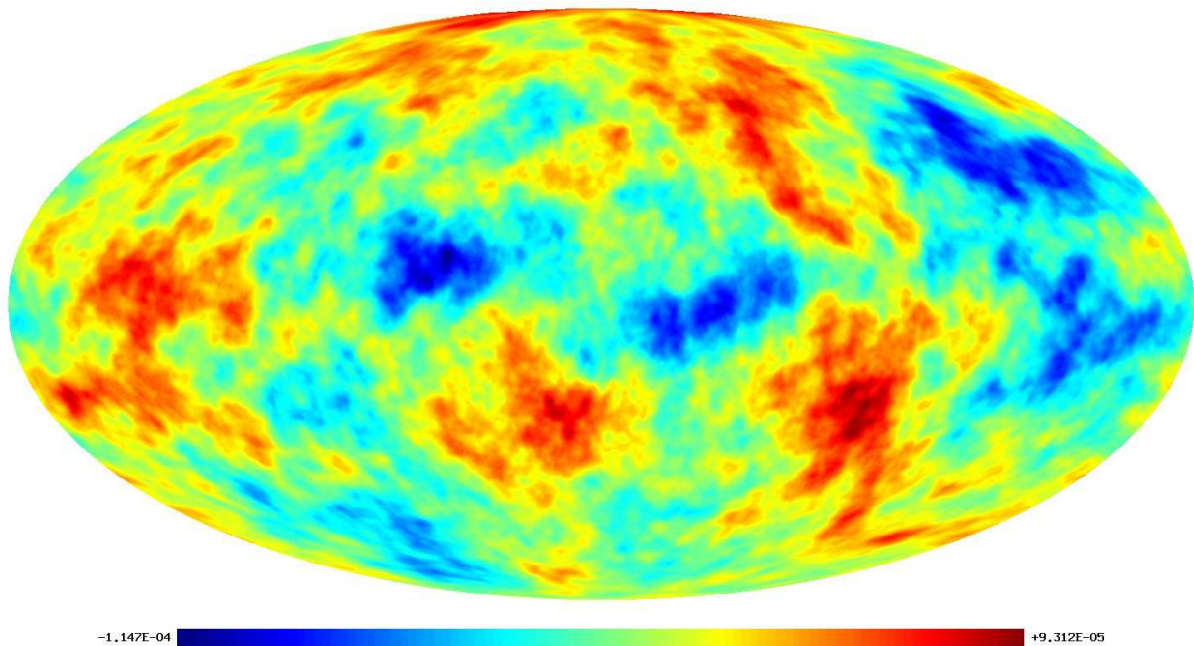
Figure 2. The simulated all-sky map of the lensing potential computed with the map-making procedure described in the text.

the B-mode polarization power on *all the scales* (Lewis 2005; Lewis & Challinor 2006).

Our map-making procedure is based on ray-tracing of the CMB photons in the Born approximation through the three-dimensional (3D) field of the peculiar gravitational potential. The latter is precomputed and stored for each of the MS output times on a Cartesian grid with a mesh of dimension 2560^3 that covers the comoving simulation box of volume $(500 \, h^{-1}\mathrm{Mpc})^3$. The gravitational potential itself has been calculated by first assigning the particles to the mesh with the clouds-in-cells mass assignment scheme. The resulting density field has then been Fourier transformed, multiplied with the Green's function of the Poisson equation in Fourier space, and then transformed back to obtain the potential. Also, a slight Gaussian smoothing on a scale r_s equal to 1.25 times the mesh size has been applied in Fourier space in order to eliminate residual anisotropies on the scale of the mesh, and a deconvolution to filter out the clouds-in-cells mass assignment kernel has been applied as well. The final potential field hence corresponds to the density field of the MS (which contains structures down to the gravitational softening length of $5 \, h^{-1}\mathrm{kpc}$) smoothed on a scale of $\simeq 200 \, h^{-1}\mathrm{kpc}$.

In order to produce mock maps that cover the past light-cone over the full sky, we stack the peculiar gravitational potential grids around the observer (which is located at $z = 0$), producing a volume which is large enough to carry out the integration over all redshifts relevant for CMB lensing. For simplicity, we only integrate out to $z_* \sim 11$ in this study, which corresponds to a comoving distance of approximately $r_* \sim 7236 \, h^{-1}\mathrm{Mpc}$ with the present choice of cosmological parameters. Indeed, the lensing power from still higher redshifts than this epoch is negligible for CMB lensing, as we will discuss in the next section. But we note that our method

could in principle be extended to still higher redshifts, up to the starting redshift $z = 127$ of the simulation.

The above implies that the simulation volume needs to be repeated roughly 14.5 times along both the positive and negative directions of the three principal Cartesian axes x, y, and z, with the origin at the observer. However, the spacing of the time outputs of the MS simulation is such that it corresponds to an average distance of $140 \, h^{-1}\mathrm{Mpc}$ (comoving) on the past light-cone. We fully exploit this time resolution and use 53 outputs of the simulation along our integration paths. In practice this means that the data corresponding to a particular output time is utilized in a spherical shell of average thickness $140 \, h^{-1}\mathrm{Mpc}$ around the observer.

The need to repeat the simulation volume due to its finite size immediately means that our maps will suffer from a deficit of lensing power on large angular scales, due to the absence of structure on scales larger than the MS box size. More importantly, a scheme is required to avoid the repetition of the same structures along the line of sight. Previous studies that constructed simulated light-cone maps for small patches of the sky typically simply randomized each of the repeated boxes along the past lightcone by applying independent random translations and reflections (e.g. Springel *et al.* 2001). However, in the present application this procedure would produce artefacts like ripples in the simulated deflection-angle field, because the gravitational field would become discontinuous at box boundaries, leading to jumps in the deflection angle. It is therefore mandatory that the simulated lensing potential of our all sky maps is everywhere continuous on the sky, which requires that the 3D tessellation of the peculiar gravitational potential is continuous transverse to every line of sight.

Our solution is to divide up the volume out to z_* into spherical shells, each of thickness $500 \, h^{-1}\mathrm{Mpc}$ comoving (obviously the innermost shell is actually a sphere of comoving
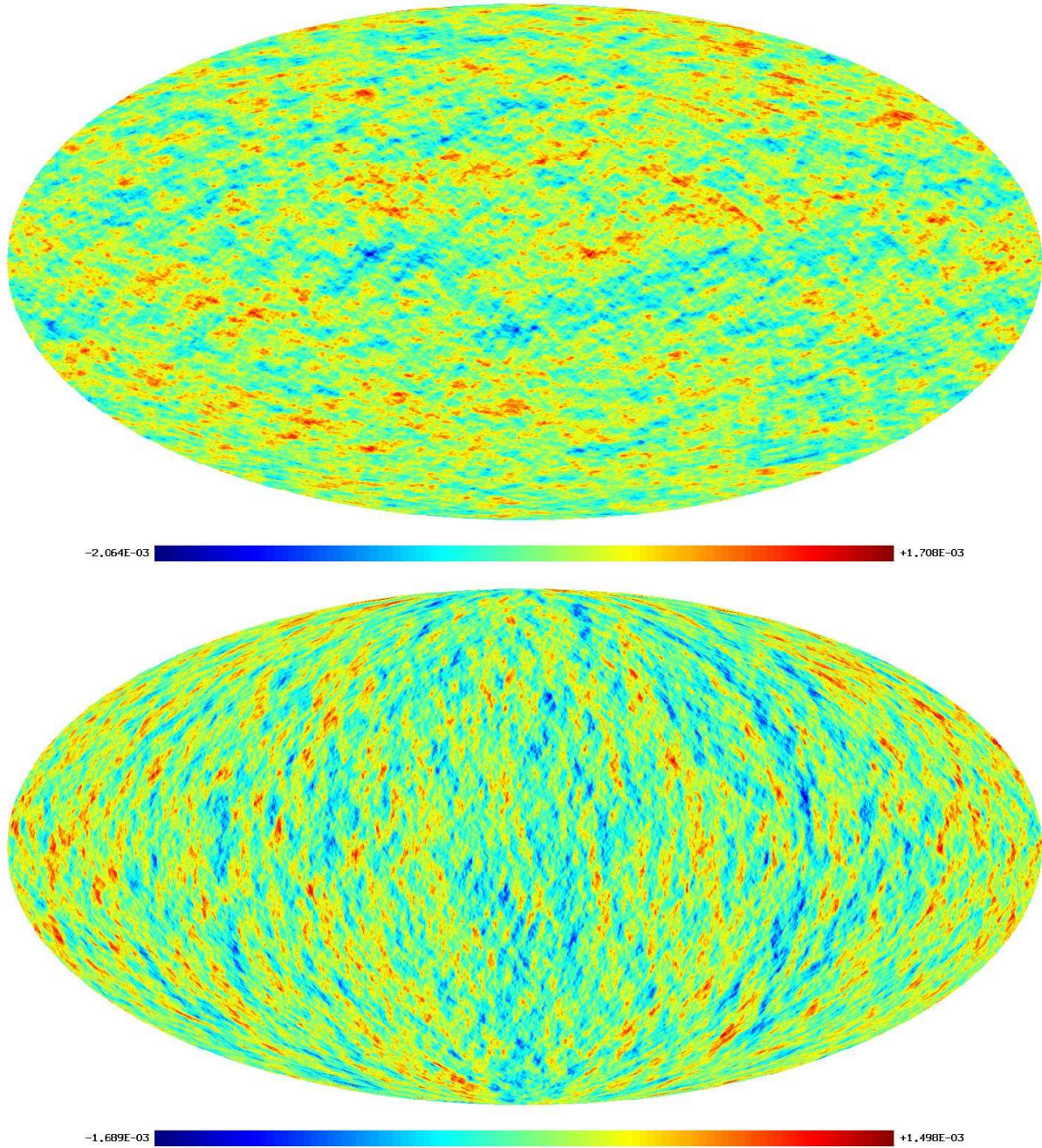
Figure 3. Simulated all-sky maps of the deflection-angle components along the ϑ direction (top panel), and along the φ direction (bottom panel), in radians.

radius $250\,h^{-1}$Mpc, centered at the observer). All the simulation boxes falling into the same shell are made to undergo the same, coherent randomization process, *i.e.* they are all translated and rotated with the same random vectors generating a homogeneous coordinate transformation throughout the shell. But this randomization changes from shell to shell. Figure 1 shows a schematic sketch of this stacking process. For simplicity, the diagram does not illustrate the additional shell structure stemming from the different output times of the simulation. As discussed before, this simply means that the underlying potential grid is updated on overage

3-4 times with a different simulation output when integrating through one of the rotated and translated $500\,h^{-1}$Mpc shells, but without changing the coordinate transformation. Notice that our stacking procedure eliminates any preferred direction in the simulated all-sky maps.

In order to define the gravitational potential at each point along a ray in direction $\hat{\mathbf{n}}$, we employ spatial trilinear interpolation in the gravitational potential grid. It is then easy to numerically calculate the integral potential for each ray, based for example on a simple trapezoidal formula, which we use in this study. Obtaining the deflection angle
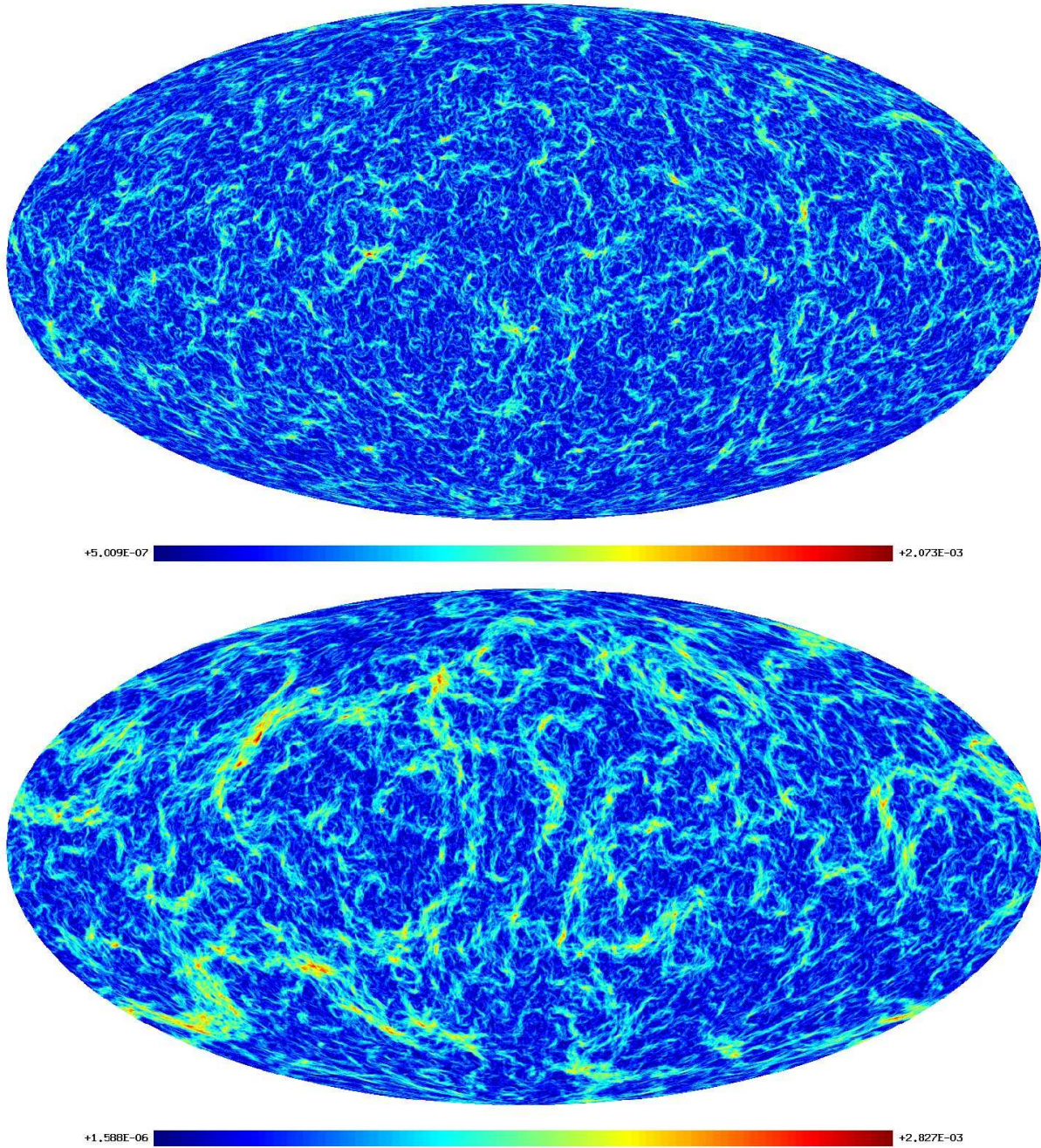
Figure 4. *Top panel*: Simulated all-sky map of the deflection-angle modulus (in radians), obtained with the map-making procedure described in the text. *Bottom panel*: Synthetic map corresponding to a Gaussian realization of the deflection-angle modulus (in radians) from the CAMB and SYNFAST codes, as described in the text.

could in principle be done by finite differencing a calculated lensing potential map, either in real space or the harmonic domain. However, the accuracy of this approach would depend critically on the angular resolution of the map. Also, the sampling of the gravitational potential in the direction transverse to the line-of-sight varies greatly with the distance from the observer, so in order to extract the maximum information from the simulation data down to the smallest resolved scales in the potential field, we prefer to directly integrate up the deflection angle vector along each light ray

in our map. For this purpose we first use a fourth-order finite-differencing scheme to compute the local 3D grid of the gradient of the gravitational potential, which is then again tri-linearly interpolated to each integration point along a line-of-sight. In this way, we calculate the deflection angle directly via equation (2) along the paths of undeflected light rays.

Finally, we need to select a pixelization of the sky with a set of directions $\hat{\mathbf{n}} \equiv (\vartheta, \varphi)$. We here follow the standard ap-
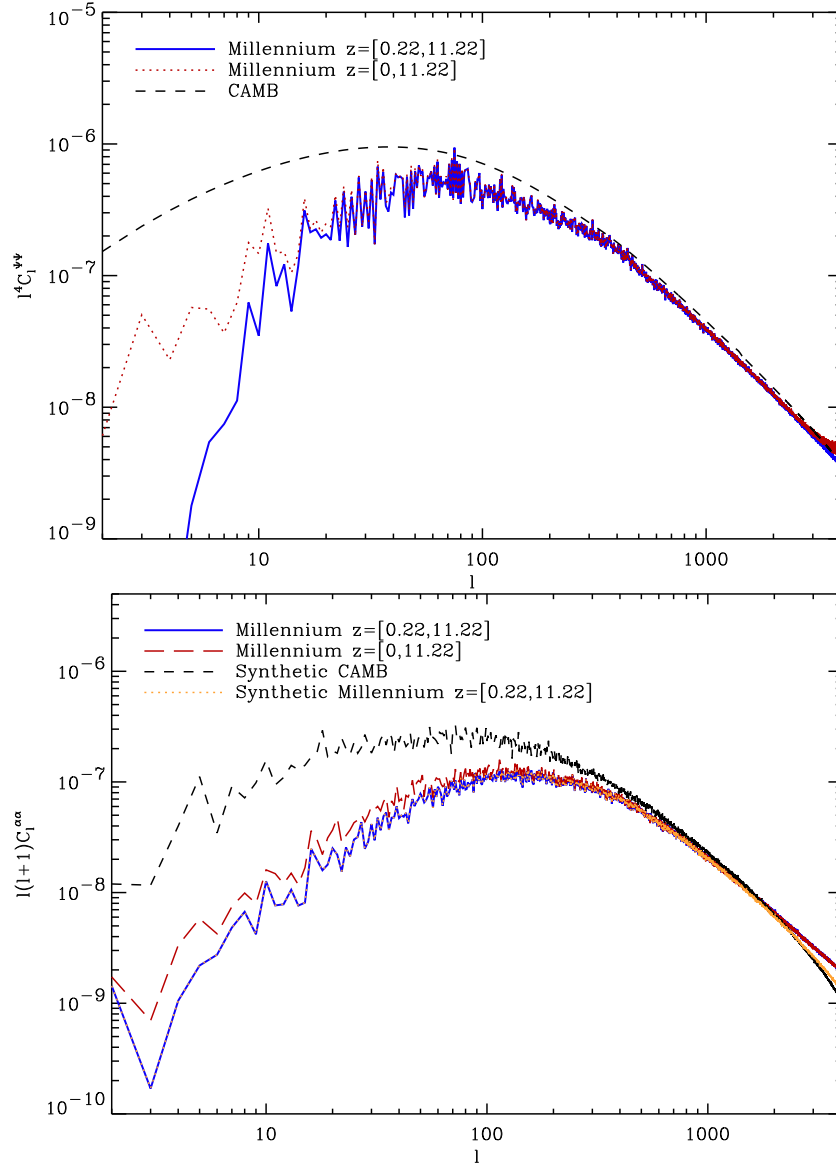
Figure 5. *Top panel*: The power spectrum of the simulated lensing potential map of Fig. 2, compared with the power spectrum of the lensing potential obtained with the CAMB code, which also includes an estimate of the non-linear contributions (Smith *et al.* 2003). The red dotted and blue solid lines differ only in the starting redshift for the line-of-sight integration used in the map-making. While the result shown in red begins at $z = 0$, the blue line gives the result for a start at $z = 0.22$. *Bottom panel*: The power spectrum (in radians squared) of the deflection angle modulus of the map shown in the upper panel of Fig. 4, compared with the power spectrum of the deflection angle modulus of the map shown in the lower panel of the same Figure. As above, the red dashed and blue solid lines differ only in the starting redshift of the line-of-sight integration, as labelled. The red dashed line is for the full redshift interval, the blue line for a start at $z = 0.22$. Moreover, the dotted orange line (corresponding to the starting redshift $z = 0.22$) represents the power spectrum of the deflection angle modulus generated with the SYNFAST code as a synthetic map corresponding to a realization constrained by the $C_l^{\Psi\Psi}$ and the $a_{l,m}^{\Psi\Psi}$ extracted by means of the ANAFAST code from a lensing potential map with starting redshift of integration $z = 0.22$, as described in the text.

proach introduced by the HEALPix[4] hierarchical tessellation of the unit sphere (Gorski *et al.* 2005).

4   SIMULATED MAPS OF THE LENSING POTENTIAL AND DEFLECTION ANGLE

In Figs. 2, 3, and 4, we show full-sky maps of the lensing potential, the deflection angle with its ϑ/φ-components, and the deflection angle modulus $|\boldsymbol{\alpha}|$, respectively, obtained with the procedures described in the previous section. The maps are generated with a HEALPix pixelization parame-
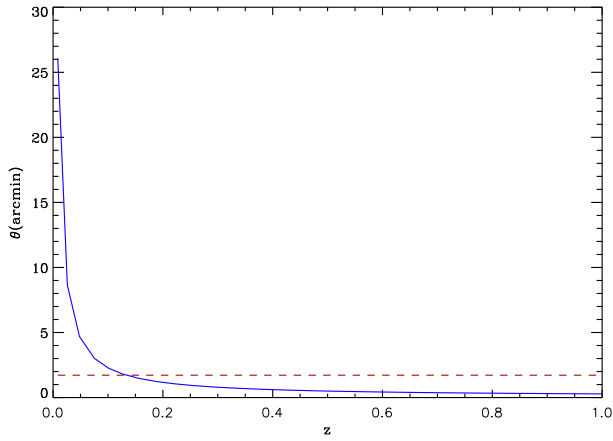
[4] healpix.jpl.nasa.gov

Figure 6. Comparison of the angular resolution of $1.72'$ of our full-sky map (red dashed line) with the redshift-dependent, effective angular resolution (blue solid line) corresponding to the intrinsic grid spacing ($\sim 200\,h^{-1}\mathrm{kpc}$) of the three-dimension gravitational potential field constructed from the Millennium Simulation.

ter $N_{\mathrm{side}} = 2048$, and have an angular resolution of $\sim 1.72'$ (Gorski *et al.* 2005), with 50331648 pixels in total.

For comparison, in Fig. 4, we also show a synthetic map of the deflection angle modulus obtained by angular differentiation of a Gaussian realization (generated with the HEALPix code SYNFAST) of the lensing potential, based on a lensing power spectrum calculated with the publicly available Code for Anisotropies in the Microwave Background (CAMB[5]), which also includes an estimate of the contribution from non-linearity (Smith *et al.* 2003).

Several interesting features should be noted in these maps. The distribution of the lensing potential appears to be dominated by large features, which are probably simply arising from the projection of the largest scale gravitational potential fluctuations along the line-of-sight. However, the strength of local lensing distortions in the CMB cannot be directly inferred from the map of the lensing potential, as for the lensing deflection only the gradient of the potential is what really matters.

The maps showing the lensing deflection angle components have interesting features as well. First of all, the signal in the two components of the deflection angle appears to possess two morphologically distinct regimes, characterized on one hand by a diffuse background distribution, caused probably by the lines-of-sight where no dominant structures are encountered, and on the other hand by sharp features, caused probably by massive CDM structures which give rise to the largest deflections in the line-of-sight integration itself. The same features are evident in the map of the modulus of the deflection-angle.

The mean value of $|\boldsymbol{\alpha}|$ in our simulated maps is $1.543'$, while its standard deviation is $0.805'$. The latter is about a factor 2 lower than the value of $\sim 1.5'$ expected from the 'semi-analytical' estimates (Bartelmann & Schneider 2001; Lewis 2005). Our interpretation is that this difference is primarily due to the lack of power on scales larger than

$500\,h^{-1}\mathrm{Mpc}$ in the MS, as it is well known that a relevant contribution to the lensing power comes from comparatively large linear scales, something that is also evident from the morphologies of the maps themselves as we discuss below.

As a first more detailed quantitative analysis, we measure the power spectra of our simulated maps and compare them with the semi-analytical expectations. We postpone the characterization of the lensing non-Gaussianity to a forthcoming and dedicated study. Using the routine ANAFAST of the HEALPix package, we have independently measured the power spectra of lensing potential ($C_l^{\Psi\Psi}$) and deflection angle modulus ($C_l^{\alpha\alpha}$) of our maps, *i.e.* without exploiting the relation between the two quantities, which holds in the spherical harmonic domain. We compare with the corresponding power spectra obtained as output from CAMB, using the cosmological parameters of the MS and with the non-linear matter power spectrum corrections of HALOFIT.

The top panel of Fig. 5 shows the primary result of this comparison. The black dashed line represents the semi-analytic prediction from CAMB as discussed above. The dotted red curve represents the result for the full integration starting at $z = 0$ and ending at $z = 11.22$. A power deficiency on large scales with respect to the semi-analytical prediction is evident, but confined to a multipole range corresponding to a one degree or more in the sky. As we now explain, the reason is the lack of structures on scales larger than the box size in our simulation. In order to prove this, we plot the solid blue line which gives the MS lensing potential power spectrum obtained from a line-of-sight integration starting at a redshift of $z = 0.22$ and ending at $z = 11.22$; comparing the two curves, a power decrease at low ℓ is easily observable in the solid blue line, with respect to the dotted red one, illustrating the influence of the lack of comoving scales greater than $500\,h^{-1}\mathrm{Mpc}$ in the MS: as the redshift increases, progressively higher multipoles are affected, increasing the power deficiency with respect to the semi-analytical expectation. As a result, for the case of the complete integration (dotted red line), the difference amounts to about ~ 1 order of magnitude at low multipoles ℓ relative to the semi-analytical expectations and is unavoidable due to the limited volume of the simulation box. As expected, this effect is also particularly evident on the multipole range corresponding to a few degrees or more, which is about the size of the MS box at the redshift most relevant for CMB lensing, i.e. $z \simeq 1$. The lack of large-scale power in the simulated maps with respect to the semi-analytical expectations is also evident by visual inspection of the upper and lower panels in Fig. 4: the features in the lower panel are on noticeably larger angular scales when compared with those in the upper panel.

However, towards larger ℓ, the deficit of large-scale power quickly decreases, and becomes negligible at scales $l \gtrsim 300$. Between this scale and $l \sim 3000$, there is quite good agreement between the MS lensing power spectrum and the semi-analytic prediction, but at $l \sim 4000$ the full MS signal for the lensing potential actually slightly exceeds the semi-analytic result. We think that in this case the effect is dominated by Poisson sampling noise from the low-redshift potential integration at $z \lesssim 0.1$. At very low redshift, the $1.72'$ angular resolution of our map is comparable and even smaller than the intrinsic angular resolution corresponding

[5] See camb.info.

to the spatial grid of the 3D gravitational potential field we use. This is evident in Fig. 6, where we compare the map's angular resolution of $1.72'$ (red dashed line) with the effective angular resolution corresponding to the intrinsic grid spacing ($195\,h^{-1}\mathrm{kpc}$) of the 3D gravitational potential field as function of redshift. Because the line-of-sight integral for the projected lensing potential involves a $1/r$ weighting term, the resulting noise terms are unfavourably amplified when the lensing potential is considered.

Physically and numerically more meaningful is the deflection angle itself, where this problem does not occur. In the bottom panel of Fig. 5, we show a comparison of the power spectrum of the deflection angle modulus ($C_l^{\alpha\alpha}$) measured for our simulated maps with the semi-analytic prediction constructed with CAMB and SYNFAST, as explained above. Again, we find a deficit of power on large scales, and a reassuring agreement over about an order of magnitude in l on intermediate scales. However, for $l \gtrsim 2000$ we find clearly more power in the deflection angle maps than anticipated by CAMB. Our map making procedure offers very good resolution at the most important redshift for lensing of the CMB, $z \sim 1$ (see also Fig. 7), where the intrinsic angular resolution of our potential grid is six times better than the angular resolution of the full-sky map. We therefore think that this higher small-scale power is a direct result of the more accurate representation of non-linear structure formation in our map simulation methodology. In fact, in our current maps we are still far from probing the most non-linear scales accessible in principle with our simulation. Those are a factor 40 smaller (namely $5\,h^{-1}\mathrm{kpc}$) than resolved by the potential grid we have employed. However, using such a fine mesh is currently impractical, and would lead to angular resolutions in full-sky maps that are unaccessible even by the Planck satellite. However, for a smaller solid-angle of the map, these scales can be probed with a different ray-tracing technique (Hilbert *et al.* 2007).

We note that the semi-analytic prediction for the power spectrum of the deflection angle modulus has been evaluated as an angular gradient in the harmonic domain of a synthetic lensing potential Gaussian map; that is accurate since in this approach we work with Fourier modes right from the start anyway. From a numerical point of view, the integral and derivative operators in Eq. (2) do however not commute, even if they analytically do, in the sense that finite differencing our measured projected potential will not necessarily give the same result as numerically integrating the deflection angle along each line of sight. The latter approach is more accurate, and has been used by us in the comparison above.

As a check, we have also computed the power spectrum of the deflection angle modulus obtained by the angular differentiation in the harmonic domain of a synthetic map corresponding to a realization constrained by the $C_l^{\Psi\Psi}$ and the spherical harmonic coefficients $a_{l,m}^{\Psi\Psi}$ extracted from a lensing potential map obtained by line-of-sight integration of the gravitational potential with a starting redshift $z = 0.22$, in order to suppress Poisson noise. The resulting power spectrum is shown as a dotted orange line in the lower panel of Fig. 5.

A slight excess of power over the semi-analytic predictions is easily seen at $l \gtrsim 3000$. It can be attributed to the non-linear evolution of the MS structures to which the deflection
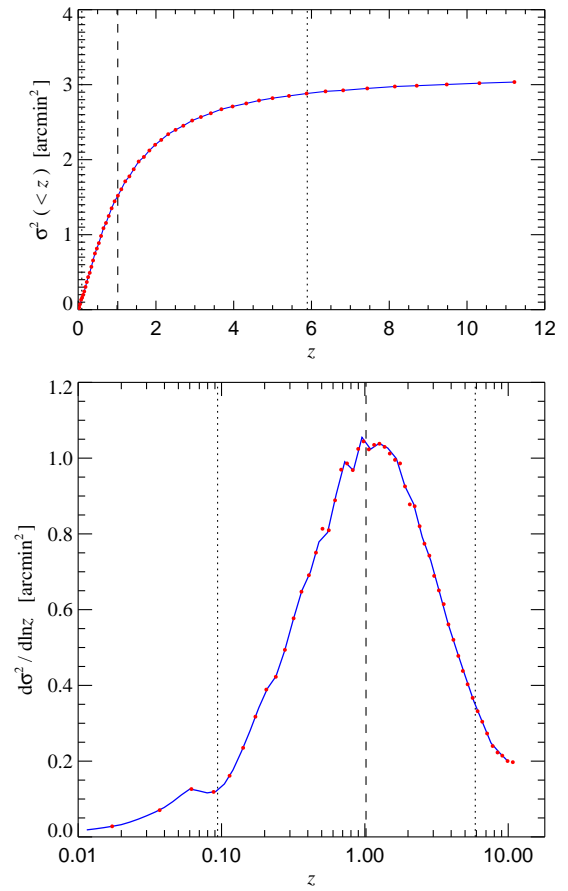

Figure 7. The cumulative and differential variance of the deflection angle map as a function of redshift. The symbols mark the different output times of the Millennium Simulation. The vertical dashed line gives the redshift that corresponds to the 50% quartile of the total variance in our maps, which is approximately at $z \sim 1$. The dotted lines mark the 5% and 95% percentiles, indicating that 90% of our signal in the deflection angle power spectrum is produced in the redshift range $z \sim 0.1$ to $z \sim 6.0$. Note however that we have lost a few percent of the total power due to our truncation of the integration at $z = 11$. When included, this would slightly shift these precentiles to higher redshift.

angle is more sensitive than the lensing potential.

On the other hand, the difference between the dotted orange line and the solid blue line at $l \gtrsim 2000$ clearly shows that our map-making approach of numerically integrating the deflection angle along each line of sight allows to preserve the contribution from the non-linear scales in a more efficient way than simply operating in the harmonic domain.

Finally, we consider the distribution of the deflection angle power along the line-of-sight. In Fig. 7, we show the cumulative and differential variance of the deflection angle as a function of redshift. We see that the most important contributions to the final signal are stemming from $z \sim 1$, i.e. about half ways between the last scattering surface and the observer, as expected. This also allows us to assess the relative error introduced by stopping the integration at $z \simeq 11$, which is of the order of a few percent.

5 CONCLUSIONS

We constructed the first all sky maps of the cosmic microwave background (CMB) weak lensing deflection angle based on a high-resolution cosmological N-body simulation, the Millennium Run Simulation (MS). The lensing potential and deflection angle are evaluated in the Born approximation by directly ray-tracing through a three-dimensional, high-resolution mesh of the evolving peculiar gravitational potential and its gradient. The time evolution is approximated by 53 simulation outputs between redshift $z = 0$ and $z \simeq 11$, each used to cover a thin redshift interval corresponding to a shell in the past light-cone around the observer. To prevent artificial repetition of structures along the line-of-sight, while at the same time avoiding discontinuities in the force transverse to a line-of-sight, we tessellate shells of comoving thickness corresponding to the size of the box $(500\,h^{-1}\mathrm{Mpc})$ with periodic replicas which are coherently rotated and translated within each shell by a random amount.

Using the Hierarchical Equal Area Latitude Pixelization (HEALPIX) package for obtaining a uniform sky-coverage, we have constructed simulated CMB lensing maps with ~ 5 million pixels and an angular resolution of $\sim 1.72'$, based on potential fields calculated on 2560^3 meshes from the Millennium simulation. In the present study, we analyze the power spectrum of the lensing potential and the deflection angle, and compare it with predictions made by semi-analytic approaches. We note that our general approach for map-making can be extended to other CMB foregrounds, including the Integrated Sachs-Wolfe (ISW) and Rees-Sciama effects at low redshifts, as well as estimates of the Sunyaev Zel'dovich (SZ) effects, or of the X-ray background. This will in particular allow studies of the cross-correlation of the lensing of CMB temperature and polarization with these effects, which will be the subject of a forthcoming study.

Our comparison of the angular power spectrum of the lensing-potential and the deflection-angle with semi-analytic expectations reveals three different regimes in our results. First, our maps show a clear deficit of power by up to an order of magnitude on scales larger than a few degrees, due to the finite size of the simulation. Second, on intermediate scales ranging from a few arcminutes to about one degree, our simulated maps produce a lensing signal that matches the semi-analytic expectation. Third, we find evidence for an excess of power in our simulated maps on scales corresponding to one arcminute and less, which we attribute to the accurate inclusion of non-linear power in the Millennium simulation. In this regime we expect our procedure to be more accurate than map-making approaches which operate in the spherical harmonic domain using semi-analytic estimates, apart from being more general. It will be especially interesting to study the non-Gaussianities in the signal we found and its implied consequences for CMB observations.

The new method proposed here demonstrates that an all-sky mapping of CMB lensing can be obtained based on modern high-resolution N-body simulations. This opens the way towards a full and accurate characterization of CMB lensing statistics, which is unaccessible beyond the power spectrum with the existing semi-analytical techniques. This is relevant in view of the forthcoming CMB probes, both as a way to detect, extract and study the CMB lensing signal, which carries hints on the early structure formation as well as the onset of cosmic acceleration, and as a tool to distinguish CMB lensing from the Gaussian contribution due to primordial gravitational fluctuations.

REFERENCES

Acquaviva V., Baccigalupi C., 2006, Phys. Rev. D **74**, 103510.

Bartelmann M., Schneider P., 2001, Phys. Rept. **340**, 291.

Colberg J.M. *et al.*, 2000, Mon. Not. R. Astron. Soc. **319**, 209.

Colless M. *et al.*, 2001, Mon. Not. R. Astron. Soc. **328**, 1039.

Evrard A.E. *et al.*, 2002, Astrophys. J. **573**, 7.

Geller M.J., Huchra J.P., 1989, Science **246**, 897.

Gorski K.M., 2005, Astrophys. J. **622**, 759.

Gott J.R.I. *et al.*, 2005, Astrophys. J. **624**, 463.

Hilbert S., White S.D.M., Hartlap J., Schneider P., 2007, Mon. Not. R. Astron. Soc. , in press.

Hirata C.M., Seljak U., 2003, Phys. Rev. D **68**, 083002.

Hu W., 2000, Phys. Rev. D **62**, 043007-1.

Hu W., Huterer D., Smith K.M., 2006, Astrophys. J. Lett. **650**, L13.

Jenkins A. *et al.*, 1998, Astrophys. J. **499**, 20.

Lewis A., 2005, Phys. Rev. D **71**, 083008.

Lewis A., Challinor A., 2006, Phys. Rept. **429**, 1.

Ma C.P., Bertschinger E., 1995, Astrophys. J. **455**, 7.

Refregier A., 2003, Annu. Rev. Astron. Astrophys. **41**, 645.

Seljak U., Hirata C.M., 2004, Phys. Rev. D **69**, 043005.

Shapiro C., Cooray A., 2006, JCAP **0603**, 007.

Smith R.E. *et al.*, The Virgo Consortium, 2003, Mon. Not. R. Astron. Soc. **341**, 1311.

Smith K.M., Zahn O., Dore O., 2007, Phys. Rev. D **76**, 043510.

Spergel D.N. *et al.*(2003), Astrophys. J. Suppl. **148**, 175.

Springel V., White M., Hernquist L., 2001, Astrophys. J. **549**, 681.

Springel V., Frenk C.S., White S.D.M., 2006, Nature **1137**, 440.

Wambsganss J., Bode P., Ostriker J.P., 2004, Astrophys. J. Lett. **606**, L93.